

Disentangling between low order telescope aberrations and segmentation errors using a Shack-Hartmann sensor

R. Mazzoleni ^{a*}, N. Yaitskova ^a, L. Noethe ^a

^aEuropean Organisation for Astronomical Research in the Southern Hemisphere
Karl-Schwarzschild-Str. 2, Garching, Germany

ABSTRACT

The shape correction of the mirrors is a crucial operation to obtain diffraction limited images in actively controlled telescopes. If the mirror is not monolithic, the segmentation errors introduced by piston, tip and tilt of the segments are superimposed on the continuous aberrations. In the case of a sensor based on the measurement of the wavefront slopes, like the Shack-Hartmann wavefront sensor, an algorithm which allows separating the different contributions is necessary for a proper correction. In the framework of the Active Phasing Experiment (APE) carried out at ESO, we have developed an algorithm to compute the continuous aberrations and the tip-tilt coefficients based on the modal wavefront reconstruction. The description of the algorithm and some examples in the cases of low-order aberrations superimposed on tip-tilt misalignment of the segments are reported, with particular emphasis about the effect of the use of a non-orthogonal set of basis functions. The precision achievable with the Shack-Hartmann sensor in APE at VLT and in the case of the European Extremely Large Telescope (E-ELT) is computed and the expected upper limits for the residual errors after correction are finally estimated.

Keywords: Segmented telescope, Shack-Hartmann sensor, active optics.

1. INTRODUCTION

The diffraction limit is the ultimate dream of the astronomer who wants to improve the spatial resolution of large telescopes. A diffuse technique implemented to achieve this limit consists in the correction of the shape of some reflecting surface in order to minimize the aberrations and restore a corrected wavefront. In the case of a segmented telescope the difficulties increase because the number of optical components to be controlled grows.

Guido Horn d'Arturo, Italian astronomer who lived during the XX century and was, for many years, director of the Bologna Observatory, faced up to these difficulties when he tried to correct the spherical aberration produced by the first segmented telescope in human history (Horn d'Arturo, 1950); his telescope, named "Telescopio a tasselli", consisted of 61 identical spherical segments with hexagonal profile, forming a primary mirror with an approximate diameter of about 1.8m; he made the correction by lifting up the segments by an amount depending on their radial distance from the central segment, in order to make the focal planes of each segment coincident; that correction allowed him to obtain images of zenithal stars with a spatial resolution of 5.6 arcseconds at the prime focus.

Today, more than half century after the realization of the first segmented telescope, we have a sufficiently developed technology to achieve the diffraction limit on segmented telescopes which are one order of magnitude larger than the "Telescopio a tasselli": currently displacement sensors and position actuators are able to measure and correct misalignments and deformations down to the level of nanometers over aperture ten meters in diameter (see Chanan et al., 1998).

One of the most common method used to compute the correction makes use of the Shack-Hartmann wavefront sensor (see Platt & Shack, 2001 for a description of the history and the historical note in Neal et al. 2002, pp. 149 about the naming convention).

The Shack-Hartmann sensor is widely used for the wavefront correction in the telescopes with monolithic mirrors. In this paper we want to present the extension of the use of this sensor to the case of a segmented telescope and to propose

* Further author information:

R. Mazzoleni: E-mail: rmazzole@eso.org, Telephone: +49 89 3200 6561

an algorithm for the wavefront reconstruction based on the modal reconstruction method; we will in particular tackle the problem of disentangling the continuous aberrations from the modes which are originated by the segmentation.

It is important to point out that the Shack-Hartmann sensor is actually a slope sensor, i.e. it is insensitive to piston; when the wavefront comes from a segmented surface, such a sensor cannot tell anything about the piston displacements; a modification which allows the detection of the relative piston step between adjacent segments has been successfully introduced at the Keck telescope (Chanan et al. 1998) and is now adopted in SHAPS within the APE experiment (see section 3.2 and Mazzoleni et al. at this conference): in that case one lenslet is located in between adjacent segments and the shape of the signal is considered rather than the centroid of the spot. In the following section we will concentrate our attention to the “classical” Shack-Hartmann and we will exclude the measure and correction of the piston displacements.

2. ALGORITHM DESCRIPTION

2.1 The extended base of functions B for the wavefront shape

Let $W(x)$ be the continuous d-dimensional ($d=1, 2$) real function defined over a d-dimensional pupil P which describes the wavefront error after the reflection on a monolithic d-dimensional mirror. Let's assume that exist a countable set of functions $\{Z_n(x): P \rightarrow \mathcal{R}\}$ which form a complete orthogonal base in the space of $W(x)$; in the case of a circular 2-dimensional pupil, $\{Z_n(x)\}$ might be, for example, the Zernike RMS-normalized polynomials (that's why the name Z_n has been chosen). $W(x)$ can be expressed in a unique way as a linear combination of the base functions, as

$$W(\bar{x}) = \sum_n a_n Z_n(\bar{x}) \quad \text{or, in the case of discrete sampling over } J \text{ points } \{x_j\} \quad W(\bar{x}_j) = \sum_n a_n Z_n(\bar{x}_j)$$

where the coefficients a_n are computed respectively as

$$a_n = \int_P W(x) \cdot Z_n(x) dx = \langle W | Z_n \rangle \quad \text{or} \quad a_n = \sum_{j=1}^J W(\bar{x}_j) \cdot Z_n(\bar{x}_j) = \langle W | Z_n \rangle$$

where P is pupil and $\langle f | g \rangle$ indicates the inner product between the functions f and g .

Let's assume that for $n \geq N$, the coefficient a_n is negligible so that the previous sum can be truncated to N :

$$W(\bar{x}) = \sum_{n=1}^N a_n Z_n(\bar{x}) \quad \text{or} \quad W(\bar{x}_j) = \sum_{n=1}^N a_n Z_n(\bar{x}_j)$$

Note that the orthogonality of the $\{Z_n(x)\}$ is, in general, not conserved over a discrete set of points.

The same set of function can be used to describe the wavefront reflected by a non-continuous surface (e.g. a segmented mirror); but, in this case, the reconstructed wavefront (and, consequently, the applied correction) might be not accurate due to the limited number of terms used in the reconstruction. The following Figure 1 illustrates qualitatively this problem in the 1-dimensional case, which refers to the case of a segmented mirror consisting of 3 segments with the central one lifted up. The wavefront after the reflection is outlined in continuous line. The reconstructed wavefront, approximated using the first 25 Zernike polynomials (dashed line), does not exactly correspond to the real one; this discrepancy might induce the wavefront correction system to apply a wrong correction: for instance, it might correct with a tilt the external segments in order to match better the reconstructed wavefront.

In order to solve this mismatching, we propose to extend the set of continuous functions $\{Z_n(x)\}$ with a set of non-continuous functions $\{S_{mk}(x)\}$ (hereinafter called also “single segment modes” of the segment k) which are real functions defined over P but are equal to 0 outside the segment k .

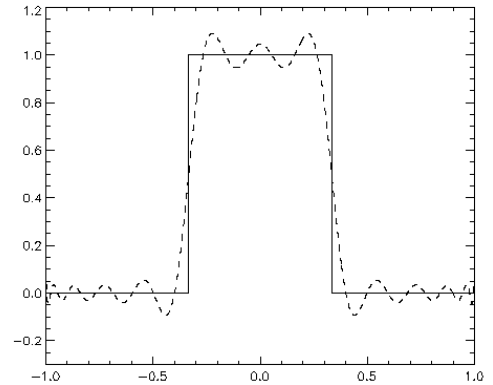


Figure 1: Piston approximation with the first 25 Zernike polynomials.

For instance, in the 1-dimensional case, $S_{1k}(x)$ and $S_{2k}(x)$ can be defined using the Zernike polynomials as:

$$S_{1k}(x_j) = \begin{cases} 1 & \text{if } x_j \in \text{Segment } k \\ 0 & \text{elsewhere} \end{cases} \quad S_{2k}(x_j) = \begin{cases} x_j - x_{0k} & \text{if } x_j \in \text{Segment } k \\ 0 & \text{elsewhere} \end{cases}$$

where x_{0k} is the coordinate of the center of the segment k . The single segment modes $S_{1k}(x)$ and $S_{2k}(x)$ correspond to the piston and to the tilt of the segment k respectively.

We assume that the first M non-continuous functions are sufficient to describe accurately the segment shape. With the new extended set of functions $B \equiv \{Z_n(x), S_{mk}(x)\}$, the following approximation for the wavefront can be used:

$$W(\bar{x}_j) = \sum_{n=1}^M a_n Z_n(\bar{x}_j) + \sum_{m=1}^M \sum_{k=1}^K b_{mk} S_{mk}(\bar{x}_j) \quad (1)$$

where M is the number of non-continuous functions and K is the number of segments.

2.2 The extended base of functions B' for the wavefront slope

The Shack-Hartmann sensor measures the local slope of the wavefront, i.e. the derivative of the wavefront with respect to the spatial coordinates in the plane of the detector. It is then necessary to reformulate the wavefront reconstruction formula (1) in terms of the derivatives and for this we need to define a new set of basis functions B' .

The derivative of the wavefront error represented by (1) with respect to the i coordinate can be written as:

$$\partial_i W(\bar{x}_j) = \sum_{n=2}^M a_n \partial_i Z_n(\bar{x}_j) + \sum_{m=2}^M \sum_{k=1}^K b_{mk} \partial_i S_{mk}(\bar{x}_j) \quad (2)$$

Note that the piston modes (the segment piston S_{1k} and the global piston Z_1 , if Zernike polynomials are used) have been removed from the sum because they cannot be detected by the Shack-Hartmann sensor being their spatial derivative equal zero. Note also that the derivative of the non-continuous functions is not defined at the segment borders but this fact can be ignored if the sampling points are inside the segments.

Among the plethora of possible choices, it seems ‘‘natural’’ to build the new set B' using the derivatives of the functions defined in B , i.e. $B' \equiv \{\bar{\partial} Z_n(x), \bar{\partial} S_{mk}(x)\}$, where each derivative is a d -dimensional vector of functions (that is $\bar{\partial} Z_n(x) = \{\partial_i Z_n(x)\}$, where i indicates the coordinate along which the derivative is computed).

The following points can be noticed:

- The new base B' is ‘‘naturally’’ defined from B in the sense that each function in B generates one function in B' (a pair of functions if $d=2$).
- Each function which can be described in B , can be derived within each segment and its derivative can be described in B' using the same coefficients a_n and b_{mk} (piston modes excluded).
- If the functions in B are linearly independent and the piston modes are excluded, then also the derivatives (considered as pair of functions if $d=2$) are linearly independent. Orthogonality, in general, is not conserved (see Noll, 1976 for case of the Zernike polynomials).

2.3 Orthogonalization.

Using the same notation of the previous paragraph, let $B' \equiv \bar{\partial} B = \{\bar{\partial} Z_n(\bar{x}_j), \bar{\partial} S_{mk}(\bar{x}_j)\}$. We assume that the functions computed over the points $\{x_j\}$ are linearly independent and that the piston modes have been removed from the original base B .

We can now define a new set of base B'' derived from B' with an orthogonalization procedure, e.g. the Gram-Schmidt procedure. From each function F'_i ($i=2, \dots, N$), selected with a specific order, a new function F''_i is derived in the following way:

$$F_i'' = F_i' - \sum_{j=0}^{i-1} \frac{\langle F_i' | F_j'' \rangle}{\|F_j''\|} \quad \text{where } \|F\| = \sqrt{\langle F | F \rangle}.$$

With this definition, each new function F''_i is orthogonal to the F''_j with $j < i$.

The orthogonalized functions F'' depend on the order in which the functions F' are listed; a proper choice of the order will reduce the computational effort needed to obtain the orthogonalized set. However the choice of the order will have no influence on the final results, i.e. the coefficients of the functions in B' will be the same independently of the chosen order.

To visualize how the choice of the order affects the orthogonalized set of functions, let us consider a simple case, with $d=1$ (mono-dimensional) and $K=3$ (3 segments).

Let $B \equiv \{S_{2k}, Z_3\}_{k=1..3}$, i.e. the 3 segment tilts plus global defocus defined over $P=[-1, 1]$ as listed in the following table together with their derivatives. The function $\theta(x, S)$, where x is a point and S a interval, is defined as being equal to 1 if x belongs to S , otherwise it is equal to 0.

Function description	Definition	Derivative
Tilt of the first segment	$S_{21}(x_j) = (x_j + 2/3) \cdot \theta(x_j, [-1, -1/3])$	$S'_{21}(x_j) = \theta(x_j, [-1, -1/3])$
Tilt of the second segment	$S_{22}(x_j) = x_j \cdot \theta(x_j,]-1/3, +1/3[)$	$S'_{22}(x_j) = \theta(x_j,]-1/3, +1/3[)$
Tilt of the third segment	$S_{23}(x_j) = (x_j - 2/3) \cdot \theta(x_j, [+1/3, +1])$	$S'_{23}(x_j) = \theta(x_j, [+1/3, +1])$
Global defocus	$Z_3(x_j) = 2 \cdot x_j^2 - 1$	$Z'_3(x_j) = 4 \cdot x_j$

The 4 derivatives $\{S'_{2k}, Z'_3\}$ in B' , are plotted in the following graphs:

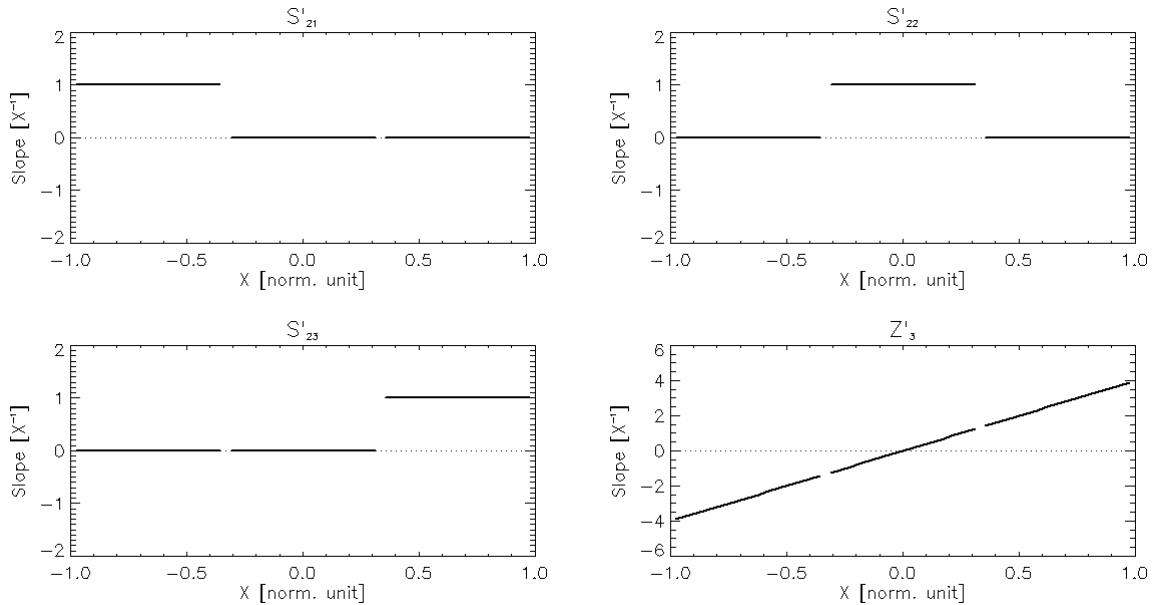


Figure 2: Derivatives of the segment tilt and global defocus.

If the order in B' is $\{S'_{2k}, Z'_3\}$ than $S''_{2k} = S'_{2k}$ and only the function Z''_3 in B'' will be modified by orthogonalization:

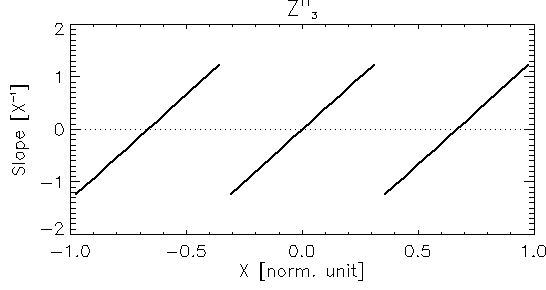


Figure 3: **Function Z''_3** after orthogonalization of $\{S'_{2k}, Z'_3\}$.

It is interesting to note that Z''_3 is the function which describes to the so called “scalping effect”.

On the contrary, if the order in B' is $\{Z'_3, S'_{2k}\}$, then $Z''_3 = Z'_3$ and $S''_{22} = S'_{22}$ while S''_{21} and S''_{23} will be modified in the way plotted in the following graphs:

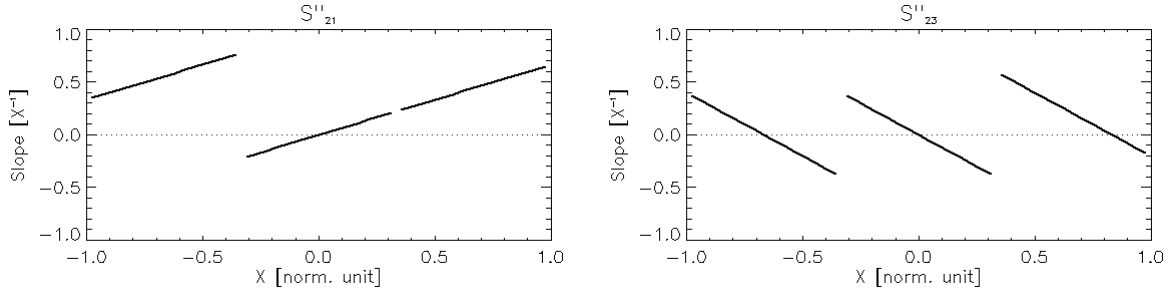


Figure 4: **Functions S''_{21} and S''_{23}** after orthogonalization of $\{Z'_3, S'_{2k}\}$.

To simplify the reading, we introduce now a new notation. Let $B' \equiv \{f_i\}_{i=1..N}$ be the base system for the wavefront slope and let $B'' \equiv \{f''_i\}_{i=1..N}$ be the base system obtained after orthonormalization.

Let M be the square matrix of order N which represents the transformation $T: B' \rightarrow B''$:

$$\vec{f}'_j = \sum_{i=1}^N M_{ij} \vec{f}_i$$

If B' is composed of linearly independent functions (as assumed), M is non-singular, it can be inverted and we can write:

$$\vec{f}_i = \sum_{j=1}^N (M^{-1})_{ij} \vec{f}'_j$$

2.4 Computation of the solution.

The equation (2), which expresses the derivative (or the derivatives) of the wavefront at the point x_j can be written as

$$\vec{d}_{\bar{x}_j} = \sum_{i=1}^N a_i \vec{f}_i(\bar{x}_j)$$

If we define the new vector $\vec{D} = [\vec{d}_{\bar{x}_1}, \vec{d}_{\bar{x}_2}, \dots, \vec{d}_{\bar{x}_j}]$ we can write the general equation in matrix format as

$$\vec{D} = F \vec{a} \quad (3)$$

where \vec{D} is the $J \cdot d$ -dimensional column vector of the displacement measured by the Shack-Hartmann sensor just defined, \vec{a} is the unknown N -dimensional column vector of the coefficients of the basis functions $\{f_i\}$ and F is the

$J \cdot d \times N$ (sensors \times modes) matrix which represents the linear transformation; the elements of i -th column of the matrix F are the $J \cdot d$ values of $\vec{f}_i(\vec{X}_j)$; in the 2-dimensional case F is:

$$F = \begin{pmatrix} f_{1x}(\vec{X}_1) & f_{2x}(\vec{X}_1) & f_{3x}(\vec{X}_1) & \dots & f_{Nx}(\vec{X}_1) \\ f_{1y}(\vec{X}_1) & f_{2y}(\vec{X}_1) & f_{3y}(\vec{X}_1) & \dots & f_{Ny}(\vec{X}_1) \\ \vdots & \vdots & \vdots & \dots & \vdots \\ f_{1x}(\vec{X}_J) & f_{2x}(\vec{X}_J) & f_{3x}(\vec{X}_J) & \dots & f_{Nx}(\vec{X}_J) \\ f_{1y}(\vec{X}_J) & f_{2y}(\vec{X}_J) & f_{3y}(\vec{X}_J) & \dots & f_{Ny}(\vec{X}_J) \end{pmatrix}$$

where the x and y indices indicate the coordinate of the derivative.

When $J \cdot d > N$, this linear system described by (3) is over-determined. In general, it is possible to find a solution for the vector of coefficients \vec{a} in a least-squares sense, i.e. with the property of minimizing the modulus of the residual error $E = \vec{D} - F \vec{a}$. This solution can be obtained in many different ways, for instance via Single Value Decomposition (SVD). If, as in our case, the matrix F has been orthogonalized into F' , then the solution can be found simply computing the projection of the displacement \vec{D} onto the orthogonalized basis vectors and then computing the component in the original basis multiplying by means of the inverse of the matrix M :

$$\vec{a} = M^{-1} F'^T \vec{D} = M^{-1} (FM)^T \vec{D} = \tilde{F} \vec{D}$$

where \tilde{F} has been introduced to indicate the pseudo-inverse of F .

2.3 Error evaluation.

The uncertainties $\delta \vec{a}$ can be evaluated starting from the error in the measurement of \vec{D} , which is the precision of the centroiding. For simplicity we assume that the precision is equal to a constant σ for all the spots. If the spatial distribution of the intensity of a spot follows a Gaussian profile, then $\sigma = FWHM / 2.35 \cdot \sqrt{N_{phot}}$, where FWHM is the Full Width at Half Maximum of the intensity distribution and N_{phot} is the number of photons detected.

The uncertainties $\delta \vec{a}$ can be computed with the error propagation formula in the linear system theory. Starting from the modes-sensors matrix F , the precision matrix E can be computed as $E = (F F^T)^{-1}$. The variance of the coefficient of the mode i can then be expressed as

$$\delta a_i^2 = E_{ii} \sigma^2,$$

where we have assumed that the centroiding errors of the individual spots are uncorrelated. In general, the element ij of the precision matrix E is the covariance between the modes i and j ; if the modes are orthogonal, $E_{ij} = 0$ when $i \neq j$.

The residual wavefront RMS over the full aperture can then be estimated taking into account the weight of each mode and the covariance between different modes.

3. APPLICATION TO 1-D AND 2-D CASES

3.1 The 1-dimensional case.

We first look at an example in the 1-dimensional case because it demonstrates how the algorithm works.

We will use the same modes as defined in the previous example of section 2.3; the segments are 3 and the modes are the 3 tilts and the global defocus; we assume that the wavefront is sampled at 6 different points, two per each segment, at the positions defined by $[r_1, r_2, r_3, r_4, r_5, r_6]$.

The modes-sensors matrix F and the $F F^T$ matrix are the following:

$$F = \begin{bmatrix} 1 & 1 & 0 & 0 & 0 & 0 \\ 0 & 0 & 1 & 1 & 0 & 0 \\ 0 & 0 & 0 & 0 & 1 & 1 \\ 4 \cdot r_1 & 4 \cdot r_2 & 4 \cdot r_3 & 4 \cdot r_4 & 4 \cdot r_5 & 4 \cdot r_6 \end{bmatrix} \quad F F^T = \begin{bmatrix} 2 & 0 & 0 & 4 \cdot (r_1 + r_2) \\ 0 & 2 & 0 & 4 \cdot (r_3 + r_4) \\ 0 & 0 & 2 & 4 \cdot (r_5 + r_6) \\ 4 \cdot (r_1 + r_2) & 4 \cdot (r_3 + r_4) & 4 \cdot (r_5 + r_6) & 16 \cdot \sum_i r_i^2 \end{bmatrix}$$

In the matrix F, rows correspond to the modes while columns correspond to the sensors.

We consider now two cases, a first one with equally spaced sampling points, that is $[r_1=-5/6, r_2=-3/6, r_3=-1/6, r_4=1/6, r_5=3/6, r_6=5/6]$ and a second with non-equally spaced sampling points, that is $[r_1=-6/6, r_2=-5/6, r_3=-1/3, r_4=1/3, r_5=5/6, r_6=6/6]$, indicated by the small triangles in the Figure 5:



Figure 5: Sampling points for the two cases illustrated in the text.

The precision matrices $E=(FF^T)^{-1}$ for the two cases are :

$$\begin{array}{l} \textit{tilt1} \\ \textit{tilt2} \\ \textit{tilt3} \\ \textit{defocus} \end{array} \begin{bmatrix} 3.17 & 0 & -2.67 & 1 \\ 0 & 0.5 & 0 & 0 \\ -2.67 & 0 & 3.17 & -1 \\ 1 & 0 & -1 & 0.37 \end{bmatrix} \quad \begin{bmatrix} 3.86 & 0 & -3.36 & 0.92 \\ 0 & 0.5 & 0 & 0 \\ -3.36 & 0 & 3.86 & -0.92 \\ 0.92 & 0 & -0.92 & 0.25 \end{bmatrix}$$

From the precision matrices, we can extract the variances of the modes and summarize them in the following table:

Mode	Equally spaced sampling	Non-equally spaced sampling
Tilt first segment	$3.17 \sigma^2$	$3.86 \sigma^2$
Tilt second segment	$0.5 \sigma^2$	$0.5 \sigma^2$
Tilt third segment	$3.17 \sigma^2$	$3.86 \sigma^2$
Global defocus	$0.37 \sigma^2$	$0.25 \sigma^2$

The following observations can be pointed out:

- the variance of the tilts of the outer segments is higher than the variance of the tilt of the central segment; this is due to the fact that the tilts of the external segment are correlated to the defocus mode: the presence of this mode affects the precision with which the tilts can be estimated;
- the variances change depending on the geometrical distribution of the sampling; in the second configuration the variance of the defocus mode is reduced, but, at the same time, the variance of the tilts of the outer segments is increased;
- a covariance term between the tilts of the outer segments and the global defocus mode, which is due to the non-orthogonality of the modes, is present in both cases;
- a covariance term between the tilts of the external segments is also present; this term is also due to the defocus mode, which introduces a cross coupling between these two modes. Note that the cross coupling between the global continuous modes has already been discussed (see Cubalchini, 1979).

3.2 The 2-dimensional case: SHAPS in APE.

APE is the Active Phasing Experiment carried out at ESO in order to study and compare the performances of different kinds of phasing sensors. A segmented mirror will be conjugated to the primary mirror of the Very Large Telescope, and four different phasing sensors will be tested in the lab and on sky under identical conditions: a Shack-Hartmann Phasing Sensor (SHAPS), a Diffraction Image Phase Sensing Instrument (DIPSI), a Pyramid Phasing Sensor (PYPS) and the Zernike Unit for Segment phasing (ZEUS) (see Yaitskova et al. 2006).

SHAPS is the sensor based on the Shack-Hartmann working principle. A lenslet array optically conjugated with the segmented mirror is inserted in the beam. The image formed in the focal plane of the lenslet array is recorded by the detector and can be used to estimate the tip-tilt of the segments and the global aberrations generated along the optical path, including the ones coming from the telescope. Special cylindrical lenslet in correspondence of the border of the segments are used to compute the piston step (see [3] and [5] for more detailed descriptions and preliminary results).

The next two pictures show the layout of the lenslet array used in SHAPS (left) and one of the images recorded during the preliminary test in laboratory (right).

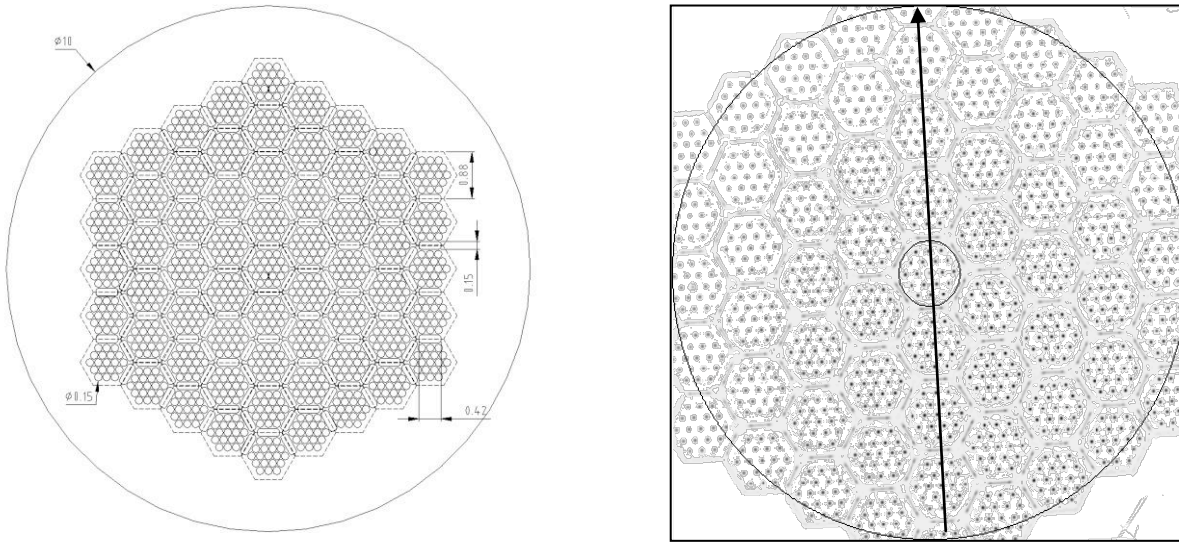


Figure 6: Layout of the SHAPS lenslet array (left) and the image formed on the focal plane (right).

The array contains $19 \cdot 61 = 1159$ lenslets, each one with a diameter of $150\mu\text{m}$ (which corresponds to 18.9 cm on the surface of the primary mirror of VLT) and focal length of 5 mm; the footprint of the VLT pupil is indicated in the right part of Figure 6 by means of two circles.

We have performed MonteCarlo simulations in order to compute the errors in the estimation of some low-order mode; the following plot shows qualitatively the decreasing of the precision (i.e. the increasing of the variance) of the measurement of the tilt of few representative segment when the global defocus mode and other continuous global modes are included. The segments chosen are the one which lie on the vertical axis plotted in Figure 6 (right), namely segments 28, 13, 4, 1, 7, 19 according to our custom numbering; they have been selected because their tilts have the highest correlation with the global defocus. Segment 0 (the central one) is excluded because it will be obscured by the secondary mirror of VLT.

The precision is computed relatively to the case in which the sole tilt modes are computed (diamonds). It can be seen that the uncertainty increases when the defocus mode is included (squares); the relative increment is higher as the distance from the center increases and where the

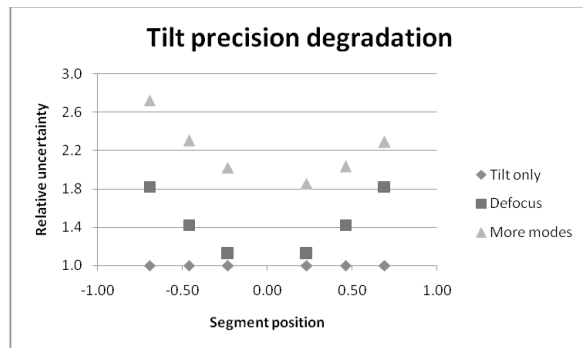


Figure 7: Variation of the tilt uncertainty in function of the distance with different configuration.

coupling between tilt and defocus is stronger. The uncertainty increases further if more modes (Coma and Astigmatism) are included in the computation (triangles). In addition introduce an asymmetry.

The residual wavefront error RMS has been estimated for the tip-tilt modes, excluding the continuous ones.

The precisions of the measure of the tilt angle of a single segment can be computed with the following formula:

$$\delta_{tilt} = \frac{\sigma}{2\sqrt{N_{phot}}} \cdot \frac{1}{M}$$

where σ is the uncertainty in the estimate of the spot centroid at the focal plane of the lenslet, N_{phot} is the number of photons detected and M is the magnification between the lenslet array and the segmented mirror. The surface error RMS due to the tilt error can be obtained as:

$$\delta_{RMS} = \frac{\delta_{tilt}}{2} \cdot s$$

where s is the segment semi-size. The two errors are plotted in Figure 8 as a function of the number of photons.

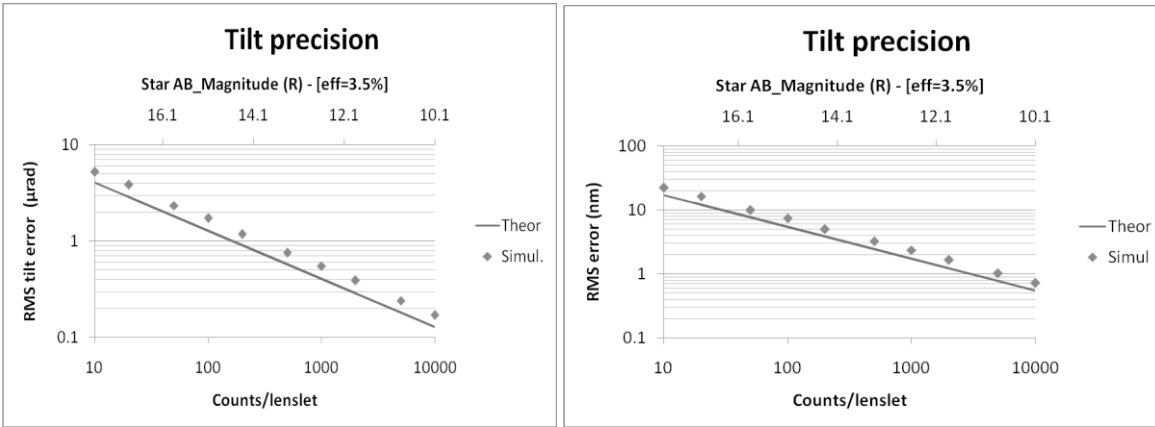


Figure 8: Tilt precision in function of the photon counts. Theoretical curve (continuous line) and simulated results (diamonds) are plotted for the segment tilt angle error (left) and for the segment RMS surface error (right).

The variable on the horizontal axis at the bottom is the number of the counts per lenslet for an integration time of 30 seconds, the variable on the horizontal axis at the top is the correspondent AB magnitudes of a star in R, assuming an overall efficiency (top of the sky – detector) of 3.5%, a reference wavelength of 650nm and a bandwidth of 50nm. The only noise considered here was the Poissonian photon noise.

Both plots show the theoretical prediction (continuous line) together with a few points obtained from MonteCarlo simulations (diamonds). The discrepancy between the prediction and the simulation is due to the fact that the algorithm which computes the centroid is not efficient and the centroid error is ~20% larger than the theoretical limit.

Counting rates from 10 to 10000 counts/lenslet, corresponding to star AB magnitudes of 17.6 and 10.1, respectively, have been considered. The tilt RMS errors for the two extreme cases are shown in the following table:

Count/lenslet/30sec	AB magnitude	Tilt angle RMS error (µrad)		Tilt surface RMS error (nm)	
		Simul.	Theor.	Simul.	Theor.
10	17.6	5.3	4.1	22.4	17.2
10000	10.1	0.2	0.1	0.7	0.5

Being the segment tip-tilts orthogonal, the residual global wavefront error RMS due just to tip-tilt errors is equal to the average wavefront error RMS of the single segment plotted in the right side of Figure 8.

The previous values refer to the case where just tip and tilts are computed. When one of the continuous modes is included, the tilt uncertainty increases, as described previously. For instance, we have estimated that when the defocus mode is included, the RMS wavefront error due just to tip-tilts increases by a factor of approximately 20%.

Finally, the residual global wavefront error RMS after defocus and tip-tilt correction can be computed as:

$$RMS^2 = RMS_{defocus}^2 + RMS_{tilts}^2 + C$$

where $RMS_{defocus}$ and RMS_{tilts} are the RMS-normalized uncertainties of the global defocus and of the tip-tilts while C is a correlation term (see the appendix for the derivation) due to the cross-coupling between defocus and tilts.

The estimated residual RMS for SHAPS is plotted in Figure 9.

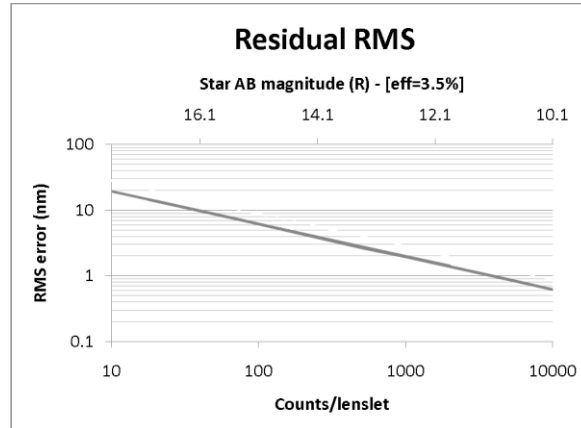


Figure 9: Expected global RMS after defocus and tip-tilt corrections.

It is important to note that the main contribution to the residual global RMS is due to piston errors. For an optimal correction the piston step of the segments should therefore be included in the list of the modes together with tip-tilt and defocus.

4 APPLICATION TO E-ELT

In the E-ELT case the primary mirror will have 984 segments, which may have tip-tilt and piston. The active correction of continuous aberrations is performed by the secondary and the tertiary mirrors. The fourth mirror is adaptive.

A Shack-Hartmann sensor for E-ELT to correct for the low-order aberrations will use M lenslets per segment, with $M \sim A/4r_0^2$, with A =area of each segment, r_0 =Fried parameter (10-20cm in the visible band) which gives $M \sim 7.5 \div 27.5$ for segment size of 1.22m (side to side).

If we assume the same configuration as used in SHAPS with 19 lenslets per segment and segment size of 1.1 m (which was in fact chosen to match the E-ELT configuration), we can apply the result obtained in the previous section. The reason is that the precisions computed for the coefficients of the tilts and the defocus, when expressed in terms of surface RMS error, are scale-invariant: they depend just on the lenslet density, i.e. the ratio between the number of lenslets within each segment and the segment area.

In that case we can estimate that the efficiency of the wavefront sensor could be a factor 10 higher than SHAPS+APE at VLT, due to the absence of APE and to the use of optimized optics and detectors. The sensor should be able to achieve the same precision as the one of SHAPS + APE at the VLT but using stars which are 10 times (i.e 2.5 magnitudes) fainter.

For what concern the cross coupling between the continuous and non-continuous mode, we expect the same effect described for SHAPS at VLT, i.e. an increase of the uncertainty in the coefficients of the modes and consequently an increase of the global residual surface error if the cross-coupling between these modes is not removed.

5 CONCLUSIONS

In this proceeding we have proposed an algorithm for the wavefront reconstruction in a segmented telescope using a Shack-Hartmann sensor.

The problem of the disentangling of a continuous mode from non-continuous ones has been tackled. In particular, we have defined a new set of basis functions, which consists of continuous and non-continuous functions; we have seen that the presence of a continuous mode together with single segment modes gives rise to a correlation which degrades the precision in the estimate of the coefficients. This effect, which is due to the non-orthogonality between the basis functions, has been illustrated with few examples. It has been shown that the degradation of the precision with which the segment tilts are computed increases when non-orthogonal continuous modes are included.

A quantitative example based on the measurements obtained with SHAPS, which is one of the wavefront sensors which is under test at ESO within the Active Phasing Experiment, has also been presented. An extrapolation to the results in the case of the E-ELT has been computed.

ACKNOWLEDGMENTS

APE is financed by the European Union and the European Southern Observatory via the Sixth European Union Framework Program for research and technological development under the contract number 011863.

REFERENCES

1. Chanan, G.A., Troy, M., et al., "Phasing the mirror segments of the Keck telescopes: the broadband phasing algorithm," *Appl. Opt.* 37, 140 (1998)
2. Cubalchini, R., "Modal wave-front estimation from phase derivative measurements," *J. Opt. Soc. Am.* 69 (7), (1979).
3. Gonte', F., et al., "Shack-Hartmann Sensor for the Active Phasing Experiment," in *Ground-based and Airborne Telescopes*, L. Stepp, ed. Proc. SPIE 6267, 626730, (2006).
4. Horn d'Arturo, G., "Altri esperimenti con lo specchio a tasselli," *Pubbl. Oss. Astr. R. Univ. Bologna*, vol. V, 11, (1950).
5. Mazzoleni, R., et al., "Design and performances of the Shack-Hartmann sensor within the Active Phasing Experiment", ref. 7012-124, this Conference.
6. Neal, D., R., Copland, J., Neal, D., "Shack-Hartmann wavefront sensor precision and accuracy," *SPIE Proceedings*, Vol. 4779, (2002).
7. Noll, R., J., "Zernike polynomials and atmospheric turbulence," *J. Opt. Soc. Am.*, Vol. 66, No. 3 (1976).
8. Platt, B., C., Shack, R., "History and Principle of Shack-Hartmann Wavefront sensing," *Journal of Refractive Surgery*, Vol. 17, (2001).
9. Yaitskova, N., & al, "The Active Phasing Experiment Part I: Concept and Objectives," in *Ground-based and Airborne Telescopes*, L. Stepp, ed. Proc. SPIE 6267, 62672Z, (2006).

APPENDIX: SURFACE RMS IN A SEGMENTED MIRROR DUE TO TIP-TILTS AND GLOBAL DEFOCUS

Consider two wavefronts, a global defocus and a segmented surface, represented respectively by:

$$\varphi_1(r) = \alpha \left[2 \left(r \frac{2}{D} \right)^2 - 1 \right] \quad \text{and} \quad \varphi_2(r) = \sum_{j=1}^N \theta(\xi_j) \left[a_{1j} \xi_{jx} \frac{\sqrt{3}}{d} + a_{2j} \xi_{jy} \frac{\sqrt{3}}{d} \right]$$

where α is the defocus amplitude in radians, r is the spatial coordinate with modulus r and components r_x and r_y , r_j is the position of the center of segment j , $\xi_j = r - r_j$ is the local spatial coordinate, a_{1j} and a_{2j} are the tip and tilt of the segment j in radians, D is the diameter of the pupil, d is the flat-to-flat width of the segment, $\theta(\xi_j)$ is the segment

characteristic function equals unit within boundary of the segment and zero outside. D , d , r and r_j are expressed with the same units.

The segments which fill the quasi-circled area are shown in Figure 10. The segment area is $A = \frac{\sqrt{3}}{2} d^2$ and the total pupil area is AN .

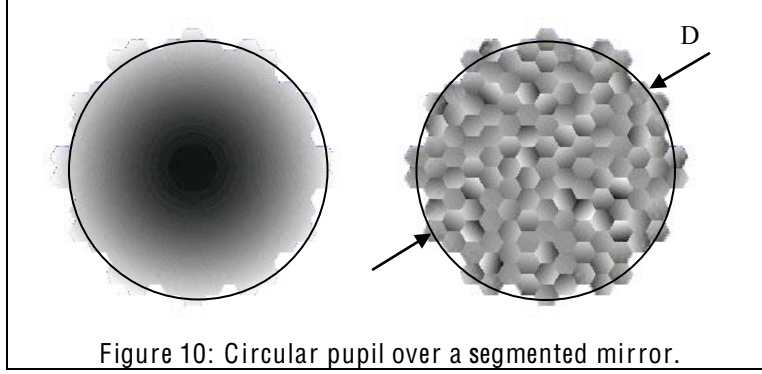


Figure 10: Circular pupil over a segmented mirror.

Consider a special set of functions, namely polynomials which are orthogonal over a hexagon with a unit radius, i.e. $\xi_j = 1$ at the corners:

$$Z_0(\xi) = 1 \quad Z_1(\xi) = \xi_x \quad Z_2(\xi) = \xi_y \quad Z_3(\xi) = 2\xi^2 - \frac{5}{6}$$

$\varphi_1(r)$ and $\varphi_2(r)$ can be represented as a combination of functions Z_i summed over the segments:

$$\varphi_1(r) = \alpha \sum_{j=1}^N \theta(\xi_j) [A_{0j} Z_0(\xi_j) + A_{1j} Z_1(\xi_j) + A_{2j} Z_2(\xi_j) + A_{3j} Z_3(\xi_j)]$$

$$\varphi_2(r) = \sum_{j=1}^N \theta(\xi_j) [a_{1j} Z_1(\xi_j) + a_{2j} Z_2(\xi_j)]$$

It can be shown that the RMS of the wavefront formed by the sum $\varphi_1(r) + \varphi_2(r)$ is given by:

$$RMS^2 = RMS_1^2 + RMS_2^2 + \frac{2}{NA_{pupil}} \int \varphi_1(r) \varphi_2(r) d^2 r = RMS_1^2 + RMS_2^2 + \frac{20}{3\sqrt{3}} \frac{d}{D^2} \frac{\alpha}{N} \sum_{j=1}^N (r_{jx} a_{1j} + r_{jy} a_{2j})$$

where RMS_1 and RMS_2 are the global RMS due to $\varphi_1(r)$ and $\varphi_2(r)$, respectively.